J Nanotechnol Nanomaterials. 2023;4(2):75-88.

Journal of Nanotechnology and Nanomaterials Research Article

Oxidation and TD-DFT of Toxic Acriflavine Hydrochloride Dye by Potassium Permanganate in Neutral Media: Kinetics and Removal of Dyes from Wastewater

Samia M. Ibrahim[1,*], Ahmed F. Al-Hossainy[1,*], Hazim M. Ali[2], Mohamed Abd El Aal[3], Nasser Farhan[1]

[1]Chemistry Department, Faculty of Science, New Valley University, El-Kharga 72511, New Valley, Egypt

[2]Department of Chemistry, College of Science, Jouf University, P.O. Box 2014, Sakaka, Aljouf Saudi Arabia

[3]Chemistry Department, Faculty of Science, Assiut University, Assiut 71516 Egypt

[*]Correspondence should be addressed to Ahmed F. Al-Hossainy, ahmed73chem@nvu.edu.eg; Samia M. Ibrahim, samiamakram2001@yahoo.com, samiamakram2001@sci.nvu.edu.eg

Received date: August 18, 2023, **Accepted date:** September 05, 2023

Citation: Ibrahim SM, Al-Hossainy AF, Ali HM, Abd El-Aal M, Farhan N. Oxidation and TD-DFT of Toxic Acriflavine Hydrochloride Dye by Potassium Permanganate in Neutral Media: Kinetics and Removal of Dyes from Wastewater. J Nanotechnol Nanomaterials. 2023;4(2):75-88.

Abstract

Fabrication of dye thin films is accomplished through physical vapor deposition with a thickness of 150 ± 5 nm. Kinetically, the reduction of permanganate ion as a multi-equivalent oxidant by acriflavine hydrochloride (ACFH) in a neutral medium has been studied spectrophotometrically. In the presence of a pseudo-first-order reaction, the experimental results suggest fractional first-order kinetics in [ACFH] and a first-order dependency in [MnO_4^-]. The spectroscopic identification of intermediate species involving complexes of Mn (V) coordination has been examined along with a unique nitro-derivative-ACF (NDACF) synthesis. Based on the estimated activation values, which are in great agreement with the kinetic data obtained, oxidation reaction mechanism was postulated and described. The data exactly determine that ΔE_g^{Opt} the amount decreases from 1.566 eV for $[ACFH]^{TF}$ to 1.36 eV for $[NDACF]^{TF}$ for isolated molecules in the gaseous state utilizing TD-DFT model, HOMO and LUMO calculation. The improvements in kinetical and optical properties were achieved, and it is promising to use $[NDACF]^{TF}$ as solar cell application.

Keywords: Acriflavine hydrochloride, Potassium permanganate, [ACFH]TF, [NDACF]TF, TDDFT, Solar cell

Introduction

To add good, necessary color that doesn't fade with light exposure, dye is a complicated chemical substance with synthetically created stable aromatic rings [1]. Coloring is usually applied in an aqueous solution and may require a mordant to increase fiber speed [2,3]. Direct skin interaction with colors has resulted in different forms of health problems such as hypersensitivity, mutagenic and carcinogenic effects, allergy and asthma, skin eczema, and immunosuppressive effects [4]. This raises concerns about how its application and exclusion from the toxicity of aqueous dye impacts and inhibits light penetration, which disrupts biological function [5,6]. Permanganate ion oxidation occurs through a number of dissimilar pathways and is classified as a multi-equivalent oxidizing agent [7]. Once more, the chemical potassium permanganate was used as an oxidizing agent to clean the water of harmful organic compounds [8] and to analyze the composition of pharmaceutical formulations. However, there has been a lot of focus on the reduction of MnO_4^- by polymers [9-12].

One hundred years ago, ACFH was first utilized as an antibacterial agent [13]. Its potential as a cancer preventative has received attention recently. Numerous cancers including colorectal, pancreatic, and prostate cancers have been linked to ACFH's antitumor activity [14]. Although its mechanism is still being studied, HIF-1 inhibition is regarded as the key anticancer strategy. It has been demonstrated that the intercalating dye ACFH prevents mitochondriogenesis. It's

an antiseptic that has been used to simultaneously detect cellular DNA and proteins using dual fluorescence. Kinetics and oxidation process of various reducing agents [15-20] by MnO_4^- have been verified elsewhere in NaOH solutions. Also, the oxidation of some compounds [21-24] by permanganate ion have previously been documented in acidic solutions. The elimination of ACFH coloring solutions by potassium permanganate was kinetically investigated in this study. The effect of reactant concentrations has been observed. The use of potassium permanganate was also carried out for the treatment of valid fabric wastewater. So, the purpose of this work is the study of the medium's effect on ACFH oxidation by permanganate ion. Once more, it was discovered that oxidation in neutral solutions occurs in two separate stages. Researchers were able to see the rather short early stage by the spectrophotometric identification of intermediary species containing complexes of Mn (V) coordination.

This study aims to provide insight into the behavior of the oxidation mechanism, the medium type of influence and reducing agent on kinetics. Another recommendation is made to make up for a lack of knowledge regarding the properties of intermediates, the type of electron-transfer process, and the transition states in the stage that controls how quickly ACFH dye is oxidized by permanganate ion. A new spectrophotometric identification of transient blue hypomanganate (V) species in the oxidation of ACFH by this oxidant using a conventional spectrophotometer is also included. This new chelating agent was created to remove toxic metal ions from contaminated materials and the environment. Notably, [ACFH] and [NDACF] ^{TF} thin films with thickness 150 ± 2 nm are created using the Physical Vapor Deposition (PVD) process. The HOMO, LUMO model is used to investigate combined fabricated thin films and DMOl^3/TDDFT-DFT for [ACFH]^{TF} and [NDACF]^{TF} samples.

Experimental Work

Materials

Without additional purification, stock solutions are used to make ACFH (Aldrich Chemical Co. Ltd.). An initial solution of ACFH was made by mixing the required quantity of reagent powder with doubly distilled water [22]. As previously reported, we prepared, standardized, and stored a $KMnO_4$ (BDH) stock solution. The reagents used in this study were analytical grade, and their solutions were made by dissolving them in doubly distilled water. To adjust the ionic strength, $NaClO_4$ was utilized as a non-complexing agent. The observed temperature is within ± 0.05 °C.

Kinetic studies

When the [ACFH] <<10 [MnO_4^-], all of the kinetic tests were conducted under pseudo-1st -order conditions. A Perkin Elmer (Lambada 750) spectrophotometer with an automatic scanning spectrophotometer fitted with a program controller and cells with a 1 cm path length was used to conduct the kinetic observations. Once more, a change in the wavelength at which permanganate ions absorb at 525 nm [23,24] or a rise in the wavelength at which they absorb at 610 nm, which is associated with the creation of the intermediate manganate (VI), was seen.

Like how **Figure 2** depicts a shift in the absorption band of the permanganate ion from 525 nm to 350 nm, the analysis occurs at the same [MnO_4^-] concentration and similar mixture concentration after 9 minutes, and the MnO_4^- band disappears to support the formation of some intermediates (**Figures 8a-8c**). In **Figure 8a**, a new band with a 390 nm wavelength can be found. These findings might imply the formation of intermediate complexes. Once more, a rise in the absorbance at 590 nm and 710 nm wavelengths reveals the formation of the intermediate species Mn (VI) and Mn (V), respectively. The reaction was shown to go through two distinct, observable phases, as seen by absorbance-time graphs. According to **Figures 8b and 8c**, the first stage was fairly and rapidly followed by the creation of intermediate coordination complexes containing transient species of blue hypomanganate (V) and green manganate (VI). The produced intermediate slowly broke down in the second slow stage, releasing soluble MnO_2 and NDACF as oxidizing substances.

Polymerization test

To investigate the possibility of free radicals forming during the reaction, 10% (v/v) acrylonitrile was added to partly oxidized reaction mixtures. We observed no polymerization was formed after a lengthy period of time.

Creation [ACFH]^{TF} and [NDACF]^{TF}

The physical vapor deposition (PVD) method was used using UNIVEX 250 Leybold (Cologne, Germany) to deposit [ACFH] and [NDACF] powder at 25°C to produce thin films with a thickness of around ≅ 150 ± 2 nm (**Figures 1a and 1b**) on quartz substrates. Numerous measuring devices for thin film thickness may be installed in UNIVEX units. The decision is based on the required automation and measurements. Systems using oscillating crystals are the norm. These can operate in UHV with or without a shutter and can have a single sensor head or several sensor heads [25,26].

Computational models

For [ACFH] and [NDACF] in the TD-DFT in gas phases state estimated evidence of PBE/GGA functionality, natural pseudo-positive preservatives, and a simple DNP set for acceptable compounds, DMol^3 calculations [27,28] results were used to determine the frequency studies and molecular structure performance. The overall value of the plane-wave power cut-out was 830 eV, according to computer simulations. For instance, the spectroscopic and physical properties of

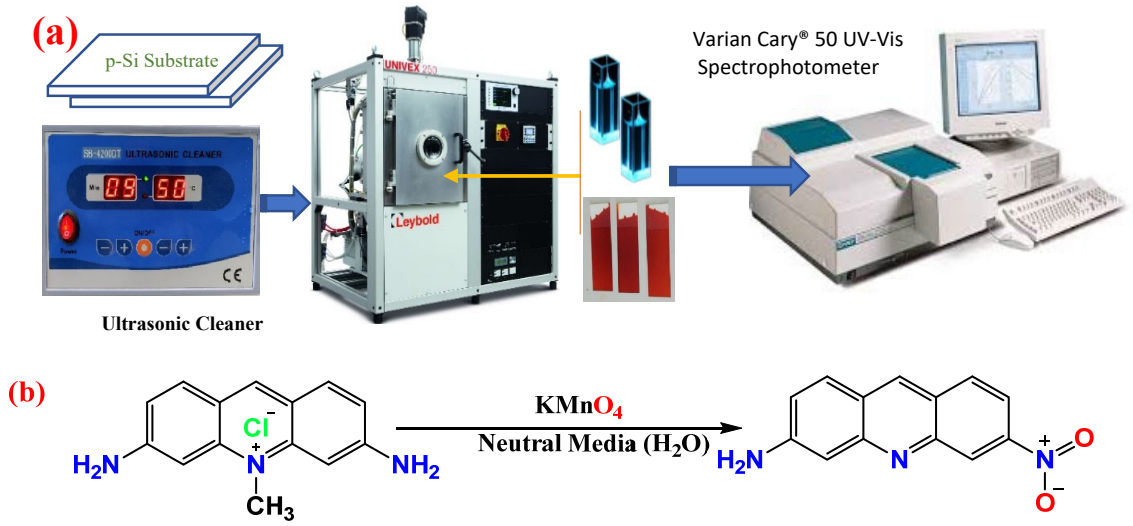

Figure 1a-b. Steps for synthesis of [ACFH]^{TF} and [NDACF]^{TF}.

[ACFH] and [NDACF] in the gaseous phase were revealed utilizing DMol^3 IR-features, which resulted in a GP frequency approximation. Additionally, it has been determined that three factors, including shape and vibrant regularity (IR), [ACFH] and [NDACF] in the gas state, and the increased nanofluid in the gaseous phase, can change how Becke [29] and Lee Yang Parr (B3LYP) [30] and WBX97XD/6-311G operate. The *GAUSSIAN 09W* method programming analyses symmetric parameters and improves the processed nanocomposite mixtures' images, power, and vibration. The WBX97XD/6-311G B3LYP method has shown a lot of helpful information regarding the connection between the setup and the range of results provided by our group [31]. The *GAUSSIAN 09W* and DMOl^3 techniques are used to assess how well [ACFH] and [NDACF] Gaussian representations in isolated molecules, deliberate changes to descriptors, prototype vitality data, and the application of numerous adjustments with varying degrees of difficulty are performed.

Results

FTIR spectroscopy data

The nitroderivative-ACF was dissolved in organic solvents and distilled H_2O. Once more, the NDACF was also characterize by the FTIR spectral bands [32,33] detected at frequencies 3299 and 3132 cm^{-1} which describe the two – NH_2 groups in ACFH, and the band at this wavenumber shifted to one peak at 3420 cm^{-1} so, this shows the oxidation reaction happens in the one amino group. Also, the peak appears at 1415, 1339, and 1320 cm^{-1} characterizing the nitro group present in **Figures 2a and 2b**. The DFT-Gaussian 09W vibration values and the experimental results are extremely comparable. After the theoretical infrared spectra of [ACFH] and [NDACF] were studied as individual molecules, spectroscopy was used to validate its presence in the gaseous phase. Expected and observed frequencies differ, as seen in **Figures 2a and 2b**. Even though the count was done in vacuum, the measurements were made to be precise in a solid-state environment. For [ACFH] and [NDACF] gaseous state of an isolated molecule and [ACFH]^{TF} and [NDACF]^{TF} thin film, the following equation has been used to define the direct correlation between the estimated ($Wn_{Cal.}$) and measured ($Wn_{Exp.}$)wavenumbers: $Wn_{Cal.} = 0.13\,\lambda_{Exp.} + 13.25$ and $Wn_{Cal.} = 0.17\lambda_{Exp.} + 14.28$ with correlation coefficients ($R^2 = 0.98\ and\ 0.99$) [25,26].

Stoichiometry and analysis of products

The stoichiometric of the entire reaction must be determined because this redox reaction is difficult and non-complementary. The stoichiometry of this reaction was discovered by mixing several molar ratios of the reactants with known concentrations at room temperature and a little excess of permanganate concentration above that of (ACFH). The concentration of the remaining (MnO_4^-) ion after the reaction (24 h) was measured using spectroscopic analysis. The ratio between ([MnO_4^-] consumed / [ACFH]$_0$) was equal to 5 mol. This result can be explained by the stoichiometric equation shown below:

$$C_{14}H_{14}N_3Cl + 5\,HMnO_4 \rightleftharpoons C_{13}H_9N_3O_2 + 5MnO_2 + CH_3OH + HCl + 2.5H_2 + 3.5O_2 \quad (1)$$

where $C_{13}H_9N_3O_2$ is ACFH and $C_{13}H_9N_3O_2$ denote as NDACF. The NDACF was identified as soluble colloidal Mn (IV) and NDACF depending on spectrum data and elemental analyses [21]. The generated Mn (IV) may be extracted by precipitates as (MnF_4) during the reaction process by adding a stoichiometric volume of F^- ions to the reaction mixtures, and then removed by filtering when the reaction is complete.

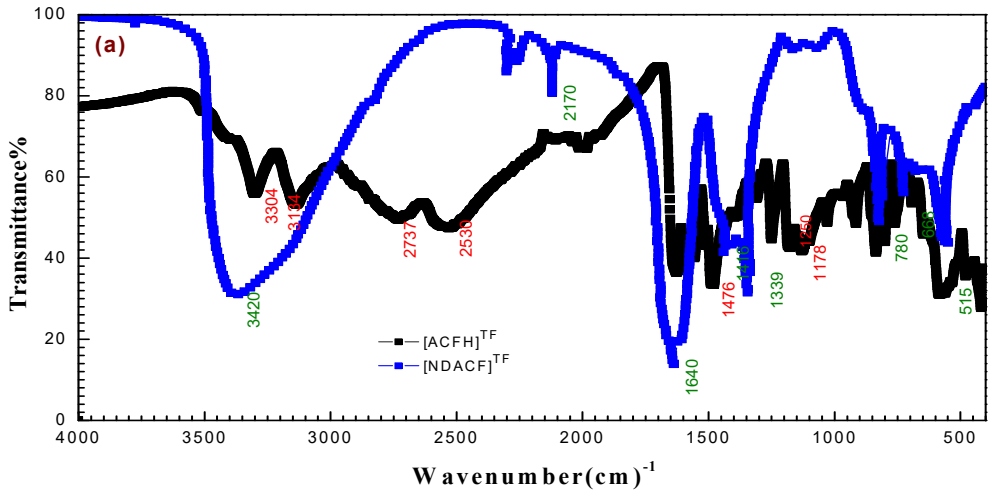

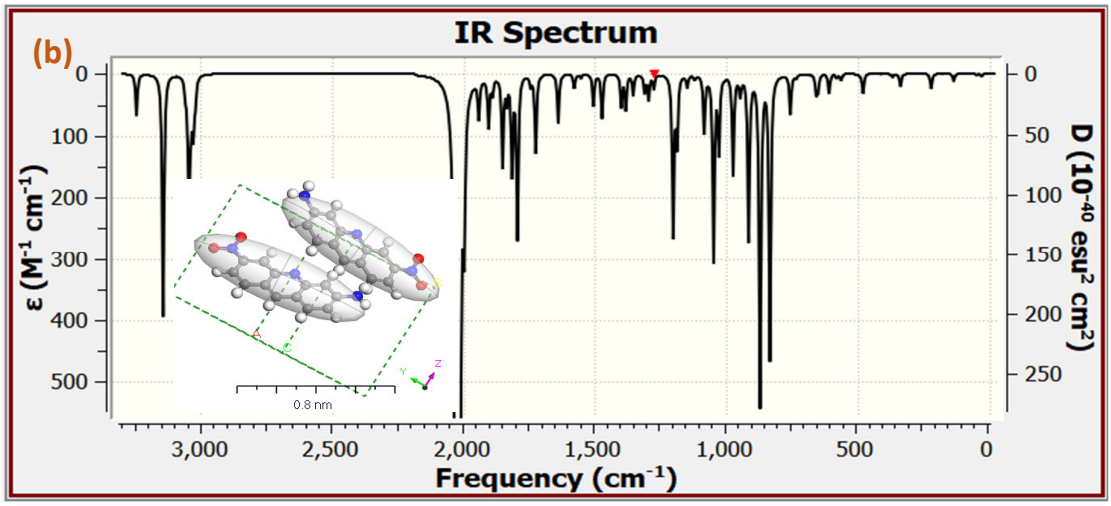

Figure 2. Collected IR data between **a)** The experimental FTIR data for the $[ACFH]^{TF}$ and $[NDACF]^{TF}$ and **b)** the simulated IR for $[ACF\text{-}NO_2]^{TF}$ isolated molecules insert is 3D of an isolated molecule in the unit cell and experimental data.

Influence of $[MnO_4^-]$ and [ACFH] on the oxidation rates

The majority of the (MnO_4^-) ion's spectrum features are displayed as it gradually disappears at the absorption maximum of 525 nm, while other species simultaneously appear in superposition at wavelengths of 605, 350, 310, and 260 nm (**Figure 3**). The pseudo-1st-order plots of the ln(absorbance) versus time relationship at the permanganate absorption maximum at λ_{max} = 525 nm showed good linearity. The identical measured pseudo-1st -order rate constants, k_{obs}, produced by the tangents of these linear plots within small experimental errors (2 ± 1) %, indicating the reproducibility of the kinetic measurements at those two wavelengths as well as the first-order reaction for the permanganate concentration.

It was demonstrated that the oxidation process exhibits first order independence of the reaction rates on the initial concentration of $[MnO_4^-]$ in the range of (1-4) x10^{-4} mol dm^{-3} in addition to the linearity of the pseudo-1st - order curves. The revelation that the reaction was first order was made possible by the independence of the reaction rates from the initial concentration of $[MnO_4^-]$ in the range of (1-4) x10^{-4} mol dm^{-3} and the linearity of the pseudo-1st -order graphs. As demonstrated in **Figure 4a**, the oxidation rates increase as the concentration of (ACFH) rises, demonstrating that the oxidation rates depend on the ACFH substrate. The Michaelis-Menten kinetics for the synthesis of a 1:1 intermediate complex was determined using a double reciprocal plot of the pseudo-first-order rate constant (k_{obs}) vs. the substrate concentration [ACFH]. A typical plot is displayed in **Figure 4b**. From the plotting of the relationship (k_{obs} = $[ACFH]^n$), a fractional -1st - order in [ACFH] was calculated (**Figure 4c**).

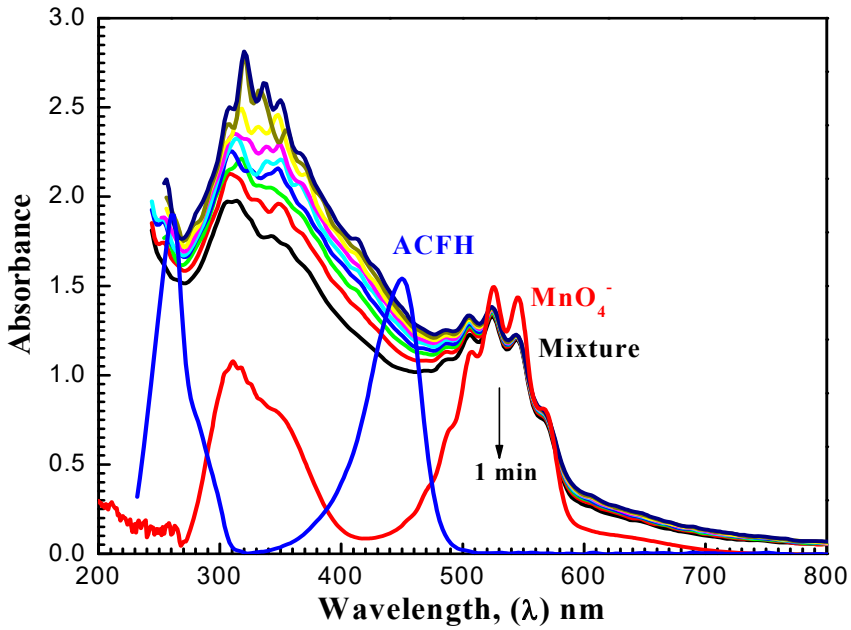

Figure 3. Spectral differences (200–800 nm) in the reduction of permanganate by ACFH in neutral medium. [MnO_4^-] = 4x10^{-4}, [ACFH] = 5x10^{-5} mol dm^{-3} at 20 °C.

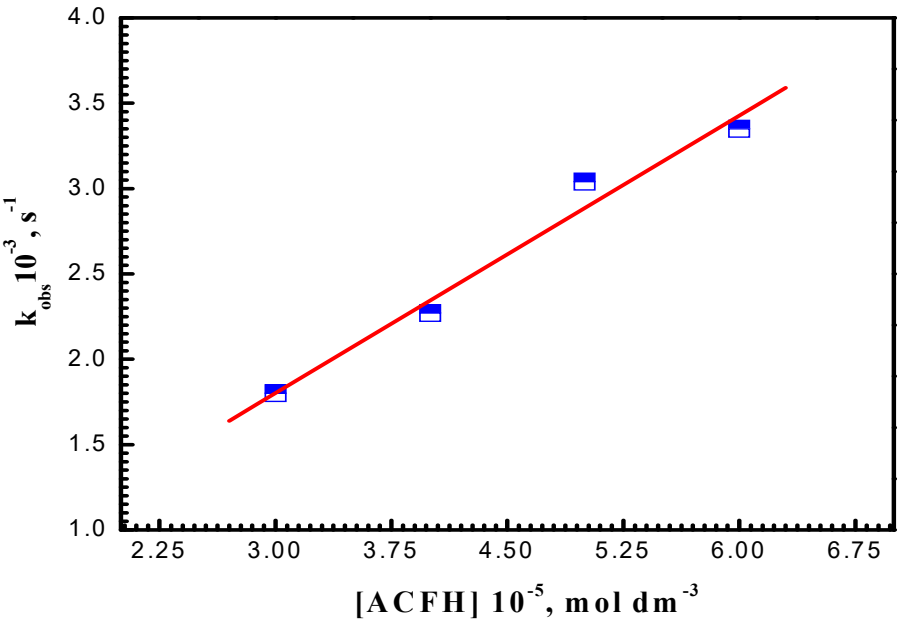

Figure 4a. Influence of [ACFH] dye on the oxidation of ACFH by permanganate ion in neutral medium. [MnO_4^-] = 4x10^{-4} moldm^{-3} at 20° C and λ= 525 nm.

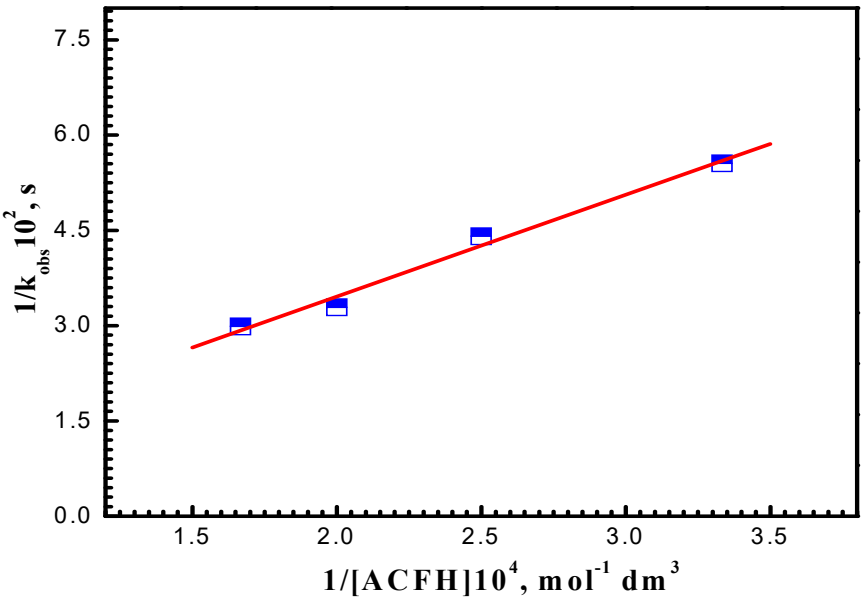

Figure 4b. A Michaelis-Menten plot of $1/k_{obs}$ vs.1/[ACFH] during the formation of the intermediate complex in the oxidation of ACFH by permanganate ion neutral medium. $[MnO_4^-] = 4x10^{-4}$ and I = 1.0 $moldm^{-3}$ at 20° C and λ= 525 nm.

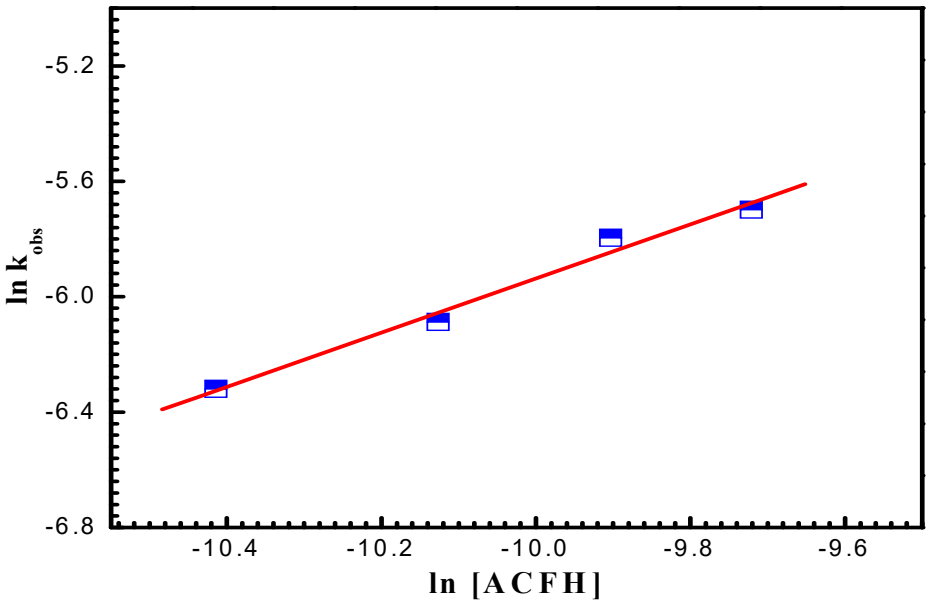

Figure 4c. A plot of ln k_{obs} against ln [ACFH] by permanganate ion in neutral medium. $[MnO_4^-] = 4x10^{-4}$ $moldm^{-3}$ at 20°C and λ= 525 nm.

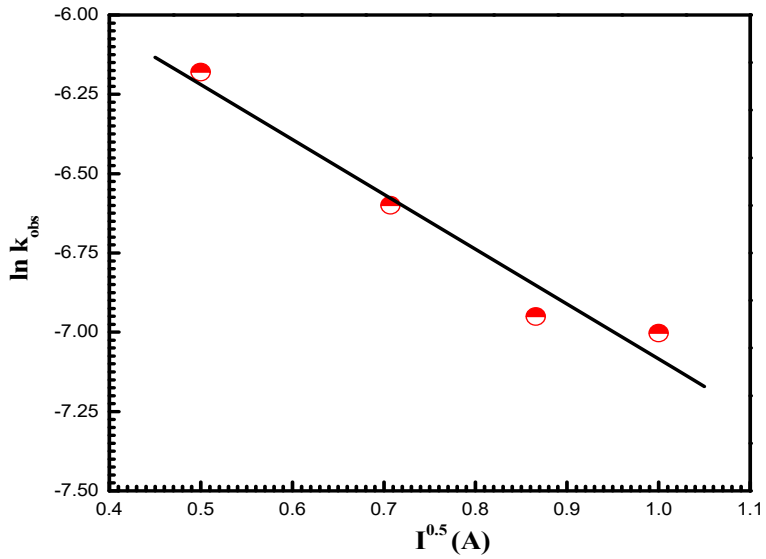

Figure 5. Debye-Huckel chart in the oxidation of ACFH by permanganate ion in neutral medium. [MnO_4^-] = 4x10^{-4}, [ACFH] = 4x10^{-5} moldm^{-3} at 20° C and λ_{max}=525 nm.

Ionic strength dependence on the oxidation rates

To comprehend the reactive species in the rate-determining stage, kinetic studies were carried out at different ionic strengths and constants of all other chemicals. It was discovered that the reaction rates producing the intermediate complex were slowed down by increasing the concentration of ($NaClO_4$) solution. It was discovered that the Debye-Hückel plot (ln k_{obs} against $I^{0.5}$ plot), which is depicted in **Figure 5**, is linear with a negative slope.

Temperature dependence on the oxidation rates

The redox method was carried out at several temperatures (at 20, 30, 40, and 50) °C, with a constant concentration of dye substrate (5x10^{-5}) mol dm^{-3}, and other reagent concentrations to determine the activation parameters of the second-order constant (k_n) in this redox technique. The experimental results revealed that when the temperature raises, the formation rate constants of intermediate complexes rise as well, matching the Arrhenius and Eyring equations.

Geometric design

Before modeling isolated molecules [ACFH] and [NDACF], several remarks concerning the effects of the positive and negative surface ratio on electron levels were analyzed. Positive surface density is maintained until it reaches the nuclear nucleus, and the number of negative components decreases, according to the Gaussian 09w /DFT. The percentage of positive regions is roughly 68% at 0.002 au, but it rises to nearly 85% with 0.01 au. **Figures 6a and 7a** indicate that the visual representations of the value MEP iso area are -15 kcal mol^{-1} and may be utilized in organic compounds. The $3D_{min}$ principles of MEP_{Vmim} are -2.237 x 10^{-1} and -1.135 x 10^{-1} kcal mol^{-1} for the [ACFH] and [NDACF] required by MEP's structure, correspondingly. Also, the $3D_{max}$ principles of MEP_{Vmax} are 5.039 x10^{-1} and 1.913 kcal mol^{-1} for the [ACFH] and [NDACF] required by MEP's structure, respectively. Since the alternative electron is present, the estimated $(MEP)_{Vmax}$ and $(MEP)_{Vmim}$ should take this into account. For this unique pair of electrons to grow, it is dependent on organic compounds for a source of alternate energy. It is simple and uncomplicated to calculate the power of a single pair using MEP_{Vmim}. The negative MEP_{Vmim}[34] the range is characterized by electron density increases in a single pair of oxygen atoms. Having an electron pull out of the cluster is also critical in order to minimize MEP_{Vmim} unwanted life. Electron impact estimations based on the number of unique kinds of organic compounds are substantially more practical and clearer than structures chloride (Cl^-) ions. [ACFH] and [NDACF] are used in the imaging of organic molecules because of their matrix donating strength. When organic compound movement is not needed, the [ACFH] and [NDACF] are substituted for just the amount of MEP_{Vmim}. In all calculations the negative value of electrostatic potential [P] of the plane of macrocyclic is symmetrical and gave positive and negative components change according to the base group. The sources (DNP) are expanded in DN to include superfluous extra extensions such as the base folder (4.4), SCF-lenience (0.0001), maximum SCF-rooms (0.5 to 102), and multi-polar Octupole, as seen in **Figures 6b and 7b**.

HOMO and LUMO are simply specifications in common reactive descriptors using quantum estimations, as shown in **Figures 6c and 7c**. The molecular balance is defined by the difference in energy between FMOs, which is essential for measuring electrical conductivity and understanding electrical transport. The values of E_H and E_L are negative and this representing that the stability of structure matrix. FMOs found in aromatic compounds are used to estimate electrophilic positions. The increases in E_H was achieved and utilizing. The differences observed in the energy band define the load transfer relationship in the molecule. So, E_g^{Opt} was representing the kinetic stability and chemically reactive. Softness and hardness are included in the stability and reactivity assessment. The highest value molecular orbital coefficients decide the location. The nucleophilic attack observed at nitrogen atoms and π-bonding in phenyl rings in HOMO (-4.536 and -4.805 eV) position and LUMO (-2.980 and -3.445 eV). E_g^{Opt} are displayed in **Figures 6c and 7c** for [ACFH] and [NDACF], correspondingly. The E_g^{Opt} for [NDACF] is lower than E_g^{Opt} for [ACFH] in isolated molecules owing to the softer and more polarizable. Even though electrons can have an accepter, soft molecules are considered reactive, as opposed to hard molecules [35]. As the device uses an electrical external charge, it predicts energy stability. HOMO (ε_H), LUMO (ε_L), E_g^{Opt}, electro-negativity (χ), chemical potential (μ), electrophilicity-index (ω), hardness (η), softness (S), ΔN_{max} and σ computed in the **Table 1.**

Numerous conformers were investigated in quantum-chemical results for the geometry of the ground stage, and the conformer with the lowest energy was selected, as proven by the harmonic vibrational frequency. The basis set superposition error was corrected for in the dimers binding energies via counterpoise correction method BSSE [36-38]. The binding energies of [ACFH] and [NDACF] in isolated molecules dimers and single molecules are tabulated in **Table 2**. So, the binding energies (ΔE_b) of the dimers were measured at the same level of theory by using the following relationship: $\Delta E_b = E_{dimer} - 2E_{monomer}$. To get a better understanding of the nature of intermolecular interactions, the TDDFT/DMOl^3 approach was used on the examined compounds and their dimers [39-41]. **Figure 8** illustrates the intermolecular interactions in the studied molecule, which contain hydrogen bonding, N-H...H--C. The lengths of the hydrogen bond are 2.671 and 3.123 Å for [ACFH] and [NDACF] as isolated molecules, respectively. On the other hand, the centroid

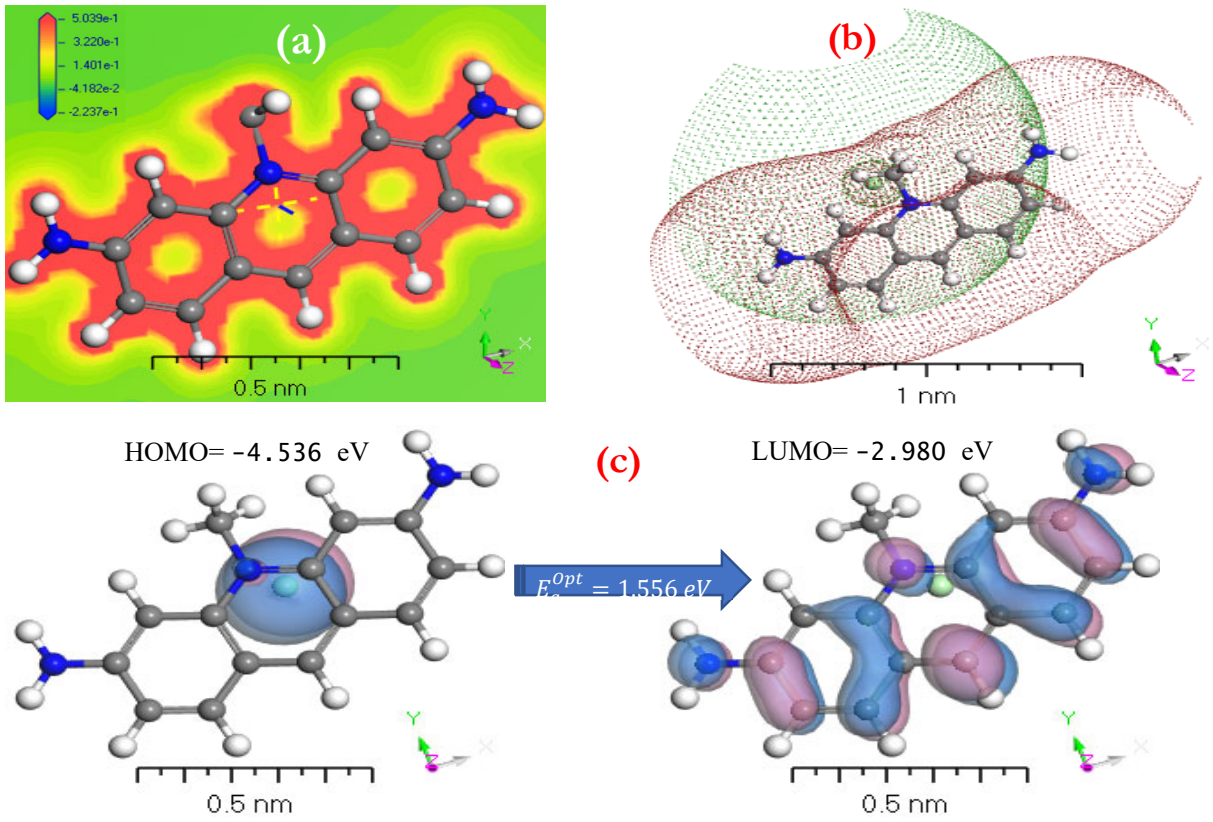

Figure 6. a) MEP; **b)** [P]; and **c)** HOMO and LUMO computations of [ACFH] isolated molecule using DMOl^3/TD-DFT technique.

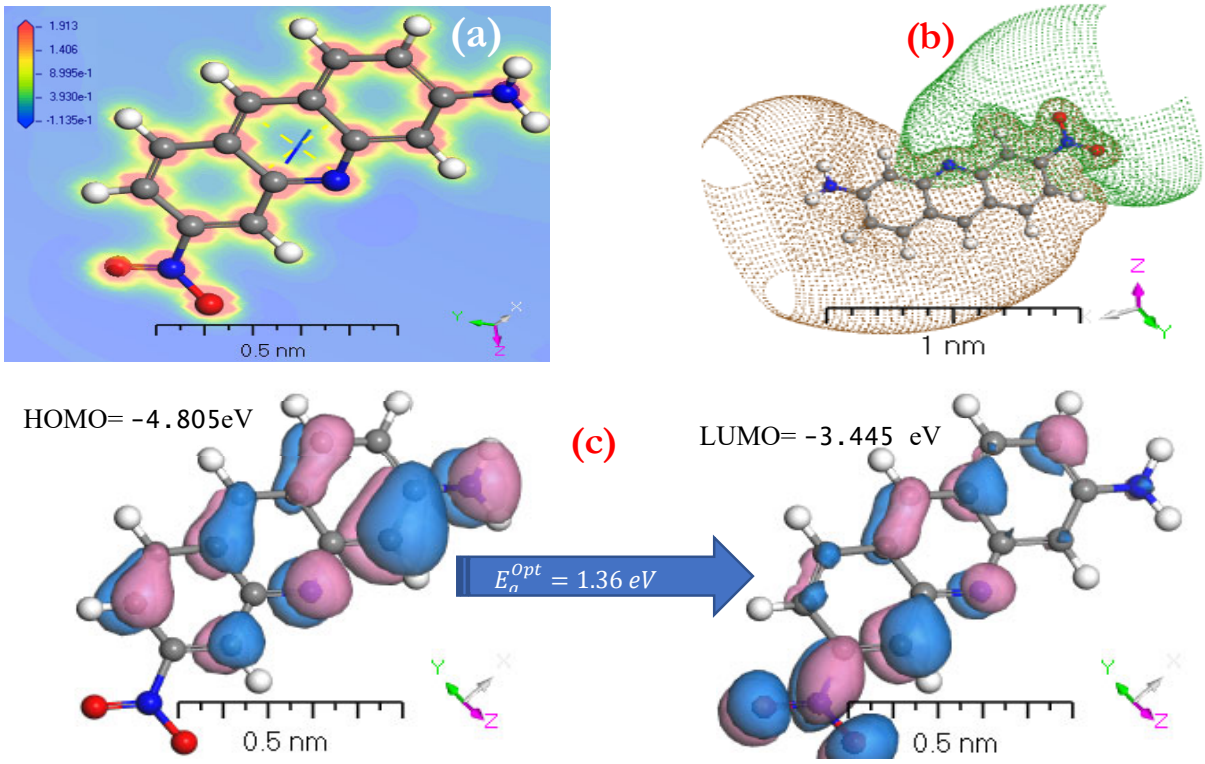

Figure 7. **a)** MEP; **b)** [P]; and **c)** HOMO and LUMO computations of [NDACF] isolated molecule using DMOl³/TD-DFT technique.

Table 1. The geometry factors/computed DMOl³/TD-DFT for [ACFH] and [NDACF] as isolated molecules.

Compound	ε_H	ε_L	$\varepsilon_H - \varepsilon_L$	χ	μ	η	S	ω	ΔN_{max}	σ
[ACFH]	-4.54	-2.98	1.56	3.76	-3.76	0.78	0.64	9.08	4.83	1.29
[NDACF]	-4.81	-3.45	1.36	4.13	-4.13	0.68	0.74	12.51	6.07	1.47
Dimer [ACFH]	-4.16	-2.89	1.27	3.52	-3.52	0.63	0.79	9.77	5.55	1.58
Dimer [NDACF]	-4.77	-3.50	1.27	4.13	-4.13	0.64	0.79	13.46	6.51	1.57

Table 2. The binding energy (E) and dimers binding energies (ΔE_b) are computed by using DMOl³/TD-DFT for [ACFH] and [NDACF] as isolated molecules. ((a)Binding Energy (kcal/mol); (b) kcal/mol; (c) Binding Bonds (BB); (d) Binding Angles (BA); (e)Centroid Binding Bonds (CBB) and (f) Centroid Binding Angles CBA.)

Compound	E_b [(a)]	ΔE_b [(b)]	BB [(c)] (Å)	BA [(d)] (°)	CBB [(e)] (Å)	CBA (°)
[ACFH]	-3778.070	13.773				
Dimer [ACFH]	-7569.913		2.671	73.80	2.706	92.44
[NDACF]	-3449.050	-4.258				
Dimer [NDACF]	-6893.842		3.123	77.128	1.577	100.88

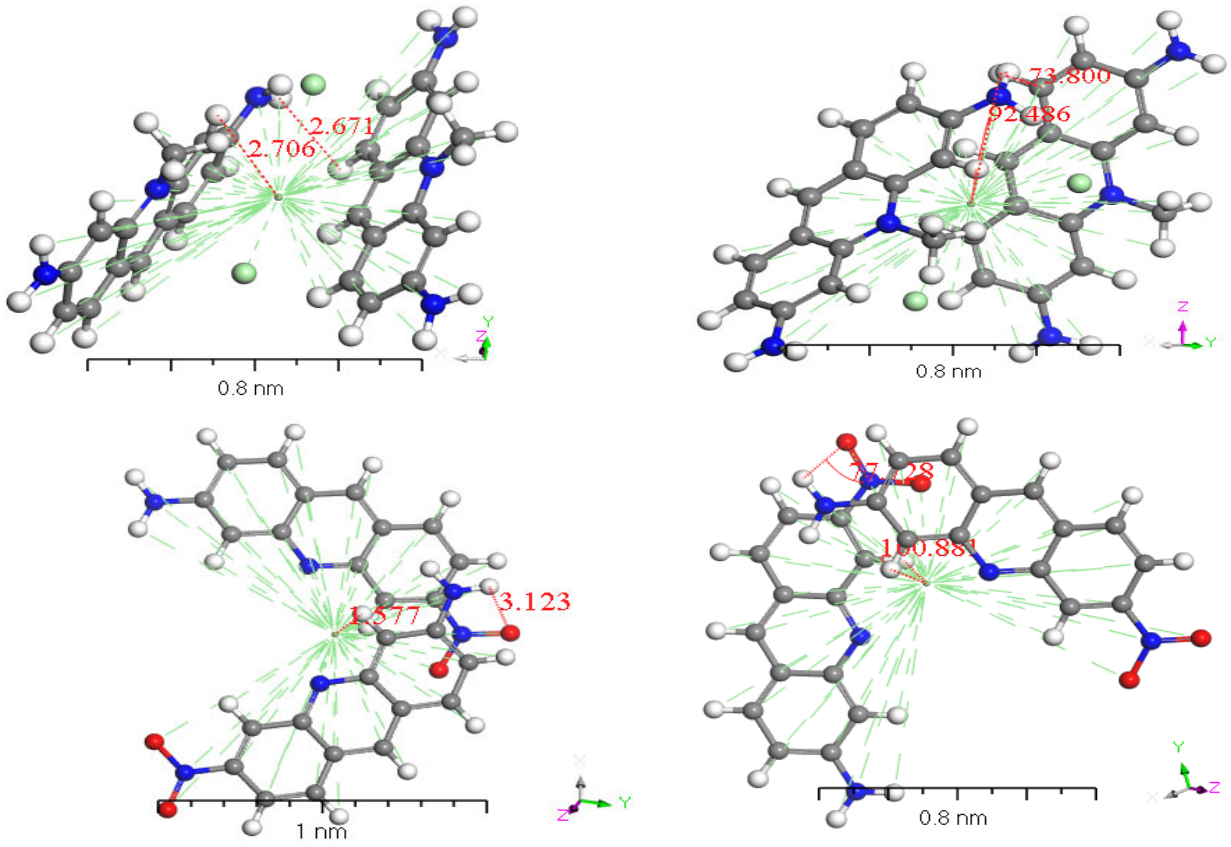

Figure 8. Stable structures for [ACFH] and [NDACF] as isolated molecules dimers in the gas phase, calculated with B3LYP/6-31+G(d,p).

lengths are 2.706 Å and 1.577 Å for [ACFH] and [NDACF] dimers isolated molecules, respectively. The dihedral angles of (N=H-H) and (N=O--H) for the [ACFH] and [NDACF] are 73.80 and 73.80° and 77.128°, respectively. Whereas the centroid length of the dimer is more than 3.50 Å, the molecule rings rotate around the centroid point [42]. It has been concluded that two isolated molecules are attached (as polymerization case) by hydrogen bond and bonding in an ACFH- 8048-52 derivatives.

Discussion

Figures 3 and **9** present various species such as hexavalent and pentavalent manganese in detail. The [MnO_4^-] band begins to gradually decrease from 525 nm, increasing in absorbance in wavelength of 605 nm. Oxidizing agents react with ACFH dye as evidenced by the development of green visible [ACFH, $Mn^{VI}O_4^{2-}$] transitional intermediate complexes with a manganate (VI) absorption band at wavelength 605 nm. Instead of the less stable Mn^{V} transient, it will show the existence of more Mn^{VI} intermediates. ($Mn^{VI}O_4^{2-}$) detection may not be very difficult due to the significantly reduced (MnO_4^- (absorption at this wavelength.

Degradation of ACFH during the oxidation using the oxidant is the attack of MnO_4^- on the ACFH formed intermediate complex (C_1) and $Mn^{V}O_3^{2-}$ followed by the creation of intermediate species (C_2) under our differences of kinetic data and this slowly decomposed intermediate complex gives final compound and MnO_2, as presented in Eqs. (2-4).

$$ACFH + MnO_4^- \overset{K_1}{\rightleftharpoons} C_1 \quad (2)$$

$$C_1 + H_2O \overset{K_2}{\rightleftharpoons} C_2 \quad (3)$$

$$C_2 \xrightarrow{k} Product + Red \quad (4)$$

As seen in the equation above, a rate law can be used to change the rate constants by raising [ACFH].

$$Rate = -d[MnO_4^-]/dt = kK_1K_2[ACFH]_T[MnO_4^-]/1 + K_2[MnO_4^-] \quad (5)$$

where $[ACFH]_T$ gives the complete analytical concentration of acriflavine hydrochloride.

The rate-law expression is:

$$Rate = -d[MnO_4^-]/dt = k_{abt}[MnO_4^-] \quad (6)$$

Comparing Eqs. (5) and (6) and rearrangement, one concludes that

$$1/k_{obs} = (1/kK_1K_2)(1/[ACFH]) + * K` \quad (7)$$

where $*K` = [MnO_4^-]/kK_1[ACFH]$. The plots of $(1/k_{obs})$ vs. (1/[ACFH]) were given straight lines from Eq. (7) with positive intercepts on the $(1/k_{obs})$ axis, and the small intercept seen in the Michaelis-Menten plot (**Figure 4b**) could be neglected.

$$[ACFH]/k_{obs} = 1/k_n = (1/kK_1K_2)(1/[ACFH]) + * K` \quad (8)$$

The elementary reaction rate constants (k) are important to understanding the electron transfer mechanism. Unfortunately, because formation constants (K_2) were not provided, some values could not be determined. However, certain efforts to extract specific values from the acquired kinetic data were performed, and the outcomes were underwhelming. Arrhenius and Eyring plots were used to assess how temperature affected oxidation rates, and the least-squares method was used to compute the activation parameters for the second-order rate constant (k_n) (**Table 3**). The manganate (VI) complex may have been compressed as shown by the significant negative values of " $\Delta S^{\neq}$" (**Table 3**). Similar to the intermediate, the intermediate is not spontaneous because both $\Delta H^{\neq}$ and $\Delta G^{\neq}$ have positive values.

According to Stewart and Coworkers [43], the value of entropy seems to be positive value so, the type of mechanism is outer-sphere reactions and more negative for inner-sphere mechanism reactions. As a result, the observed $\Delta S^{\neq}$ values may be seen as proof to support the building of inner-sphere intermediate for the transmission of electron mechanism in the current research.

The spectrum modification disruption suggests that the oxidation reaction's initial fast stage may not actually represent the stage of electron propagation (**Figure 3**). Therefore, the initial rapid phase of oxidation may be predicted due to the quick creation of an intermediate between the reactants. The creation of intermediate complexes is indicated by the appearance of a new band at 350 nm. Once more, a number of studies have been carried out to find intermediate hypomanganate (V) production as a transitory species. As can be observed in **Figure. 9b**, we were able to observe the creation of intermediate Mn(V) species while also observing an increase in the absorption at 710 nm. According to Scheme I, permanganate can be suggested as a potential preliminary reaction tool for the oxidation of ACFH in neutral solutions based on the kinetic concepts and results of the analysis described above.

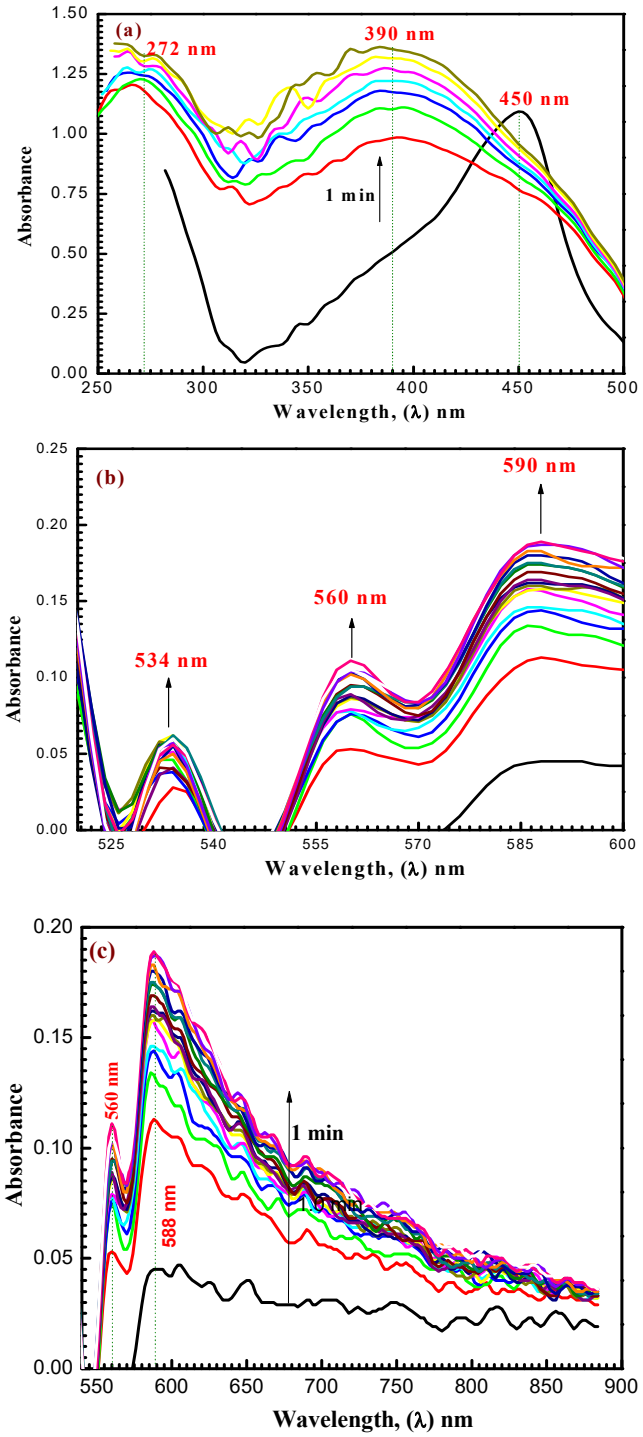

Figure 9 (a-c). Absorbance against wavelength (200–900 nm) in the reduction of oxidizing agent by ACFH in neutral. $[MnO_4^-]$= $4x10^{-4}$, [ACFH] = $5x10^{-5}$ mol dm^{-3} at 20 °C ($[MnO_4^-]$= $4x10^{-4}$). Time intervals= 1.0 min.

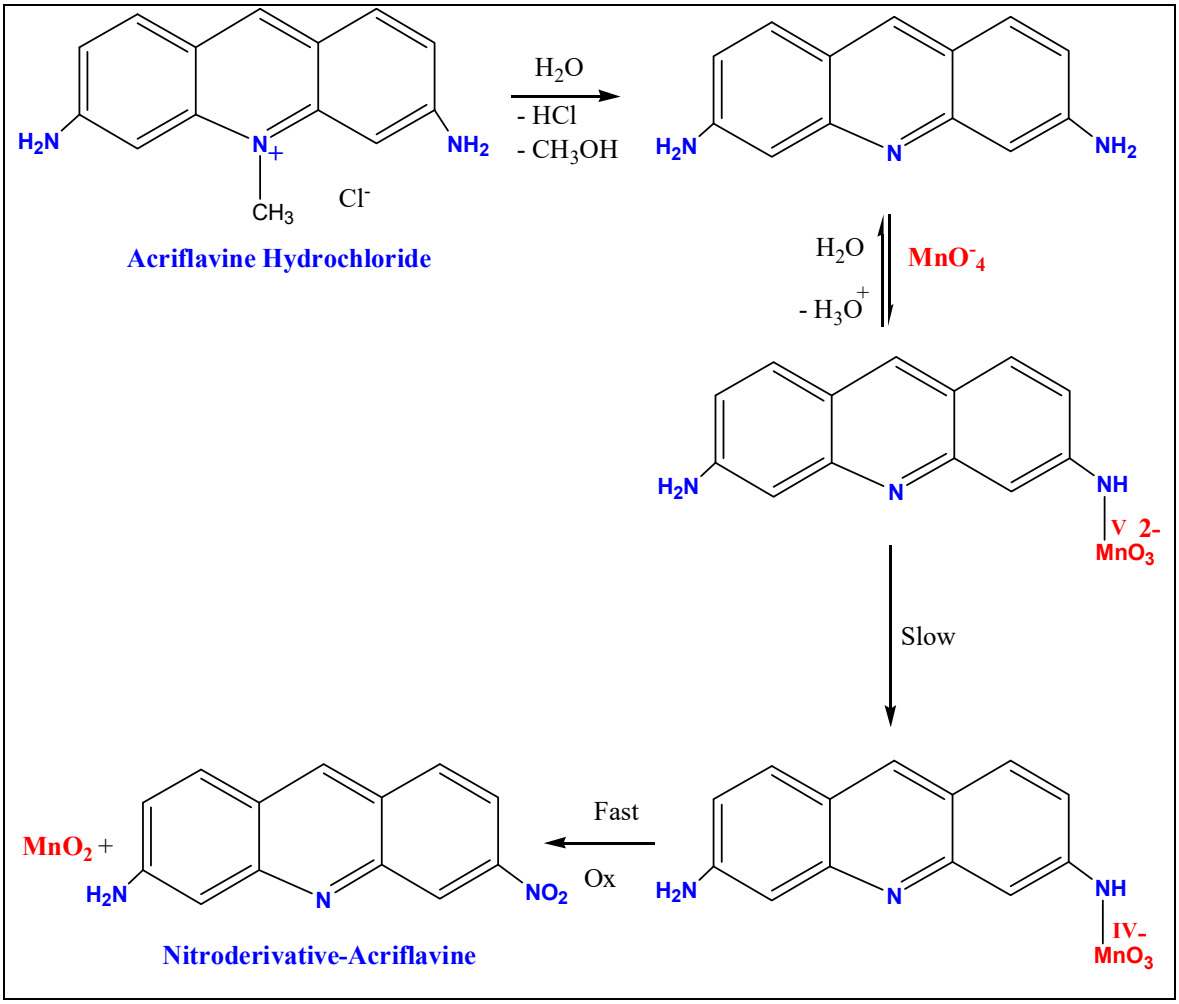

Scheme I. Mechanism of oxidation reaction between (ACFH) and permanganate ions in neutral solutions.

Table 3. Activation parameters of the second-order rate constant (k_n) in the reduction of permanganate ion by ACFH in neutral medium. [MnO_4^-]= 4x10^{-4} and [ACFH] =5x10^{-5} moldm^{-3} at λ =525 nm.

Constants	**Parameters**			
k_n	**$\Delta H^{\neq}$ kJmol^{-1}**	**$\Delta S^{\neq}$ Jmol^{-1}K^{-1}**	**$\Delta G^{\neq}_{303}$ kJmol^{-1}**	**$E_a^{\neq}$ kJmol^{-1}**
	17.95	-148.83	45.11	20.51
Error (± 3 %)				

Conclusions

By using Ultraviolet-Visible spectra, the redox system of acriflavine hydrochloride fluorescent dye with MnO_4^- at pH~7 was applied. The main results are described as follows:

- A shift in the absorption spectrum at max=710 nm that we noticed suggests that intermediate hypomanganate (V) is developing as a transient species. Thus, the rapid formation of intermediates by oxidation in neutral solutions succeeds in removing toxic colors from wastewater using permanganate ion and this appears in the Figure of spectral changes.
- The nanostructure [ACFH]^{TF} and [NDACF]^{TF} thin films have been fabricated by using the PVD method. DFT is calculated using the software DFT for *Material Studio 7.0 software*, based on simulated analysis, HOMO, LUMO, and MEP for acriflavine 8048-52 derivatives.

- The ratio percentage between the E_g^{Opt} values for [NDACF]^{TF} and [ACFH]^{TF} decreased 46.58 % this leads to [NDACF]^{TF} nanostructure more efficiency as removal of dyes from wastewater.

Credit Author Statement

Samia M. Ibrahim: Conceptualization, Modeling, Software, Review, Editing and Writing the paper. **Ahmed F. Al-Hossainy:** Conceptualization, Modeling, Software, Review, Editing and Writing the paper. **Nasser Farhan:** Review and Editing. **Hazim M. Ali:** Review and Editing. **Mohamed Abd El-Aal:** Conceptualization, Modeling, Software, Review, Editing and Writing the paper.

Conflict of Interest

The authors declare no conflict of interest.

Data Availability Statement

The data that support the findings of this study are available from the corresponding author upon reasonable request.

Acknowledgments

This work was supported by the Chemistry Department, Faculty of Science, New Valley University, El-Kharga 72511, New Valley, Egypt.

References

1. Ibrahim MB, Sani S. Comparative isotherms studies on adsorptive removal of Congo red from wastewater by watermelon rinds and neem-tree leaves. Open Journal of Physical Chemistry. 2014 Oct 15;4(04):139-46.

2. Nale BY, Kagbu JA, Uzairu A, Nwankwere ET, Saidu S, Musa H. Kinetic and equilibrium studies of the adsorption of lead (II) and nickel (II) ions from aqueous solutions on activated carbon prepared from maize cob. Der Chemica Sinica. 2012;3(2):302-12.

3. Abubakar SI, Ibrahim MB. Adsorption of bromophenol blue and bromothymol blue dyes onto raw maize cob. Bayero Journal of Pure and Applied Sciences. 2018;11(1):273-81.

4. Omran AR, Baiee MA, Juda SA, Salman JM, AlKaim AF. Removal of Congo red dye from aqueous solution using a new adsorbent surface developed from aquatic plant (Phragmites australis). International Journal of ChemTech Research. 2016;9(4):334-42.

5. Alwan RM, Kadhim QA, Sahan KM, Ali RA, Mahdi RJ, Kassim NA, et al. Synthesis of zinc oxide nanoparticles via sol–gel route and their characterization. Nanoscience and Nanotechnology. 2015;5(1):1-6.

6. Hassan KH, Mahdi ER. Synthesis and characterization of copper, iron oxide nanoparticles used to remove lead from aquous solution. Asian Journal of Applied Sciences. 2016 Jun 16;4(3):730-738.

7. Zaafarany IA. Kinetics and mechanism of oxidation of nicotine by permanganate ion in acid perchlorate solutions. International Journal of Chemistry. 2010 Aug 1;2(2):193-200.

8. Liu CS, Shih K, Wang F. Oxidative decomposition of perfluorooctanesulfonate in water by permanganate. Separation and Purification Technology. 2012 Mar 5;87:95-100.

9. Hassan R, Dahy AR, Ibrahim S, Zaafarany I, Fawzy A. Oxidation of some macromolecules. Kinetics and mechanism of oxidation of methyl cellulose polysaccharide by permanganate ion in acid perchlorate solutions. Industrial & Engineering Chemistry Research. 2012 Apr 18;51(15):5424-32.

10. Hassan RM, Ibrahim SM, Khairou KS. Kinetics and mechanism of oxidation of pyruvate by permanganate ion in aqueous perchlorate solution. Transition Metal Chemistry. 2018 Nov;43:683-91.

11. Hassan RM. Alginate polyelectrolyte ionotropic gels. XVIII. Oxidation of alginate polysaccharide by potassium permanganate in alkaline solutions: Kinetics of decomposition of intermediate complex. Journal of Polymer Science Part A: Polymer Chemistry. 1993 Apr;31(5):1147-51.

12. Khairou KS, Hassan RM. Pectate polyelectrolyte ionotropic gels: 1. Kinetics and mechanisms of formation of manganate (VI)–pectate intermediate complex during the oxidation of pectate polysaccharide by alkaline permanganate. European Polymer Journal. 2000 Sep 1;36(9):2021-30.

13. Wainwright M. Acridine—a neglected antibacterial chromophore. Journal of Antimicrobial Chemotherapy. 2001 Jan 1;47(1):1-13.

14. Dekervel J, Bulle A, Windmolders P, Lambrechts D, Van Cutsem E, Verslype C, et al. Acriflavine inhibits acquired drug resistance by blocking the epithelial-to-mesenchymal transition and the unfolded protein response. Translational Oncology. 2017 Feb 1;10(1):59-69.

15. Ibrahim SM, Saad N, Ahmed MM, Abd El–Aal M. Novel synthesis of antibacterial pyrone derivatives using kinetics and mechanism of oxidation of azithromycin by alkaline permanganate. Bioorganic Chemistry. 2022 Feb 1;119:105553.

16. Hassan RM. Alginate polyelectrolyte ionotropic gels. XIV. Kinetics and mechanism of formation of intermediate complex during the oxidation of alginate polysaccharide by alkaline permanganate with a spectrophotometric evidence of manganate (VI) transient species. Journal of Polymer Science Part A: Polymer Chemistry. 1993 Jan;31(1):51-9.

17. Shaker AM. Base-catalyzed oxidation of carboxymethyl-cellulose polymer by permanganate: 1. Kinetics and mechanism of formation of a manganate (VI) transient species complex. Journal of Colloid and Interface Science. 2001 Jan 15;233(2):197-204.

18. Hassan RM, Abdel-Kader DA, Ahmed SM, Fawzy A, Zaafarany IA, Asghar BH, et al. Acid-catalyzed oxidation of carboxymethyl cellulose. Kinetics and mechanism of permanganate oxidation of carboxymethyl cellulose in acid perchlorate solutions. Catalysis Communications. 2009 Nov 25;11(3):184-90.

19. Zaafarany I, Gobouri A, Hassan R. Oxidation of some sulfated

carbohydrates: Kinetics and mechanism of oxidation of chondroitin-4-sulfate by alkaline permanganate with novel synthesis of coordination biopolymer precursor. Journal of Materials Science Research. 2013 Oct 1;2(4):23.

20. Al-Hossainy AF, Ibrahim SM. Oxidation process and kinetics of bromothymol blue by alkaline permanganate. International Journal of Chemical Kinetics. 2021 May;53(5):675-84.

21. Ibrahim SM, Al-Hossainy AF. Kinetics and mechanism of oxidation of bromothymol blue by permanganate ion in acidic medium: application to textile industrial wastewater treatment. Journal of Molecular Liquids. 2020 Nov 15;318:114041.

22. Hassan R, Ibrahim SM. Kinetics and mechanism of permanganate oxidation of ADA in aqueous perchlorate solutions. Current Organocatalysis. 2019 Jan 1;6(1):52-60.

23. Hassan RM, Sayed SA, Ibrahim SM. Base-catalyzed oxidation of poly (ethylene glycol) by alkaline permanganate: Part I. Kinetics and mechanism of formation of coordination intermediate complex. Egyptian Journal of Petroleum. 2021 Jun 1;30(2):1-7.

24. Hassan RM, Sayed SA, Ibrahim SM. Base-catalyzed oxidation of poly (ethylene glycol) by alkaline permanganate: Part II. Kinetics and mechanistic of decomposition of coordination intermediate complex. Egyptian Journal of Petroleum. 2021 Sep 1;30(3):1-6.

25. Mahmoud SA, Al-Dumiri AA, Al-Hossainy AF. Combined experimental and DFT-TDDFT computational studies of doped [PoDA+ PpT/ZrO2] C nanofiber composites and its applications. Vacuum. 2020 Dec 1;182:109777.

26. Ibrahim SM, Bourezgui A, Al-Hossainy AF. Novel synthesis, DFT and investigation of the optical and electrical properties of carboxymethyl cellulose/thiobarbituric acid/copper oxide [CMC+ TBA/CuO] C nanocomposite film. Journal of Polymer Research. 2020 Sep;27(9):264.

27. Al-Hossainy AF, Abdelaal RM, El Sayed WN. Novel synthesis, structure characterization, DFT and investigation of the optical properties of cyanine dye/zinc oxide [4-CHMQI/ZnO] C nanocomposite thin film. Journal of Molecular Structure. 2021 Jan 15;1224:128989.

28. Ibrahim SM, Al-Hossainy AF. Synthesis, structural characterization, DFT, kinetics and mechanism of oxidation of bromothymol blue: application to textile industrial wastewater treatment. Chemical Papers. 2021 Jan;75:297-309.

29. Mohamed NS, Ahmed MM, Yahia A, Ibrahim SM, Al-Hossainy AF. Development of azithromycin–Pd mono nanocomposite: Synthesis, physicochemical, characterization and TD-DFT calculations. Journal of Molecular Structure. 2022 Sep 5;1263:133126.

30. Abd El-Aal M, Mogharbel RT, Ibrahim A, Almutlaq N, Zoromba MS, Al-Hossainy AF, et al. Synthesis, characterization, and photosensitizer applications for dye-based on ZrO2-acriflavine nanocomposite thin film [ZrO2+ ACF] C. Journal of Molecular Structure. 2022 Feb 15;1250:131827.

31. Abdel-Aziz MH, Zwawi M, Al-Hossainy AF, Zoromba MS. Conducting polymer thin film for optoelectronic devices applications. Polymers for Advanced Technologies. 2021 Jun;32(6):2588-96.

32. Abd-Elmageed AA, Ibrahim SM, Bourezgui A, Al-Hossainy AF. Synthesis, DFT studies, fabrication, and optical characterization of the [ZnCMC] TF polymer (organic/inorganic) as an optoelectronic device. New Journal of Chemistry. 2020;44(20):8621-37.

33. Ibrahim SM, Bourezgui A, Abd-Elmageed AA, Kacem I, Al-Hossainy AF. Structural and optical characterization of novel [ZnKCMC] TF for optoelectronic device applications. Journal of Materials Science: Materials in Electronics. 2020 Jun;31:8690-704.

34. Fontanals N, Borrull F, Marcé RM. Overview of mixed-mode ion-exchange materials in the extraction of organic compounds. Analytica Chimica Acta. 2020 Jun 22;1117:89-107.

35. Al-Hossainy AF, Sediq AY, Mahmoud SA. Combined Experimental and DFT-TDDFT Characterization Studies of Crystalline Mesoporous-Assembled [ZrO 2] NPs and [DPPP+ Gly/ZrO 2] C Nanocomposite Thin Film. Electronic Materials Letters. 2021 Mar;17:188-206.

36. Chong DP, Aplincourt P, Bureau C. DFT Calculations of Core− Electron Binding Energies of the Peptide Bond. The Journal of Physical Chemistry A. 2002 Jan 17;106(2):356-62.

37. Grimme S, Antony J, Ehrlich S, Krieg H. A consistent and accurate ab initio parametrization of density functional dispersion correction (DFT-D) for the 94 elements H-Pu. The Journal of Chemical Physics. 2010 Apr 21;132(15).

38. El Azab IH, Thabet HK, Almotairi SA, Saleh MG, Mogharbel RT, Mahmoud SA, et al. Synthesis of a novel coumarin heterocyclic derivative and fabrication of hybrid nanocomposite thin film with CoOFe2O4 for optoelectronic applications. Journal of Molecular Structure. 2021 Oct 5;1241:130640.

39. Mansour H, Abd El. Halium EM, Alrasheedi NF, Zoromba MS, Al-Hossainy AF. Combined experimental and TDDFT computational studies of the optical and electrical characteristic of luminol films-doped TiO2 with 9.027% power conversion efficiency. Journal of Materials Science: Materials in Electronics. 2022 Mar;33(8):5244-64.

40. El Azab IH, Gobouri AA, Altalhi TA, El-Sheshtawy HS, Almutlaq N, Maddah HA, et al. Synthesis, characterization, DFT-TDDFT calculations and optical properties of a novel pyrazole-1, 2, 3-triazole hybrid thin film. Optik. 2021 Dec 1;247:167971.

41. El Azab IH, Ibrahim A, Abdel El-Moneim M, Zoromba MS, Abdel-Aziz MH, Bassyouni M, et al. A combined experimental and TDDFT-DFT investigation of structural and optical properties of novel pyrazole-1, 2, 3-triazole hybrids as optoelectronic devices. Phase Transitions. 2021 Nov 2;94(11):794-814.

42. Li Q, Li Z. The strong light-emission materials in the aggregated state: what happens from a single molecule to the collective group. Advanced Science. 2017 Jul;4(7):1600484.

43. Lee AY, Stewart JD, Clardy J, Ganem B. New insight into the catalytic mechanism of chorismate mutases from structural studies. Chemistry & Biology. 1995 Apr 1;2(4):195-203.